Title:

Quasi-static 3D structure of graphene ripple measured using aberration-corrected TEM

Authors:

Yuhiro Segawa,[a,*] Kenji Yamazaki,[a] Jun Yamasaki,[b,c] Kazutoshi Gohara[a,*]

[a]*Division of Applied Physics, Graduate School of Engineering, Hokkaido University, Sapporo 063-8628, Japan;* [b]*Research Center for Ultra-High Voltage Electron Microscopy, Osaka University, 7-1, Mihogaoka, Ibaraki, Osaka 567-0047, Japan;* [c]*Institute of Materials and Systems for Sustainability, Nagoya University, Furo-cho, Chikusa, Nagoya 464-8601, Japan*

KEYWORDS:

graphene, ripple, aberration-corrected TEM, 3D reconstruction

*Corresponding author. Tel: +81-11-706-7331. E-mail: yuhiro26@eis.hokudai.ac.jp (Yuhiro Segawa)

*Corresponding author. Tel: +81-11-706-6636. E-mail: gohara@eng.hokudai.ac.jp (Kazutoshi Gohara)

ABSTRACT

Free-standing graphene has a three-dimensional (3D) structure, called a ripple, rather than a perfect two-dimensional (2D) crystal. Since theoretical calculations suggest that a ripple strongly influences various fundamental physicochemical properties of graphene, it is important to clarify the ripple structure quantitatively in experiments. This paper proposes a new method of measuring the 3D atomic structure of a ripple by using aberration-corrected transmission electron microscopy (TEM). The method utilizes the fact that the 2D contrast of a TEM image is sensitive to the height of a six-membered ring. The proposed method is experimentally applied to a monolayer graphene, and the 3D atomic arrangements of consecutively acquired TEM images are reconstructed. In that experiment, the specimen is found to be moving upward. Furthermore, the atomic arrangement can be approximated as a composite of two structures consisting of a 3D ripple and a 2D plane. The ripple is represented as a superposition of sinusoidal waves, with their wave vectors coinciding with the specific direction of the six-membered ring. The time dependences of the height and lateral size of the ripple are also measured.

Introduction

Graphene is a two-dimensional (2D) crystal in which hexagonal lattice structures composed of sp^2 bonds of carbon atoms are arranged [1]. On the other hand, it is known to have a three-dimensional (3D) structure that deviates from a completely flat 2D structure and that is classified into three types, depending on size: ripple, wrinkle, and crumple, with the ripple being the smallest [2]. The existence of the ripple structure was first revealed in an experiment [3]. That analysis of electron diffraction patterns of free-standing monolayer graphene revealed the existence of a ripple with a height and lateral size of about 0.5 nm and 5 nm, respectively. Monte Carlo simulations supported the results of that experiment [4]. The ripple's effects on graphene properties have also been reported [5–7].

There are two main kinds of reports on the origin of the ripple. One kind focuses on an intrinsic property that eliminates the thermodynamic instability of graphene [4,6]. The other focuses on extrinsic properties such as defects and grain boundaries in graphene [8–10], the structure of a substrate supporting graphene [11,12], or the tension applied from the substrates [13]. Moreover, whether the ripple is static or dynamic has been a subject of studies. Transmission electron microscopy (TEM) measurements of electron diffraction patterns revealed that ripples are static [3]. The first measurement by scanning tunneling microscopy (STM) concluded that a ripple is static because similar structures were observed repeatedly [14]. On the other hand, in a study that used STM to observe the movement of one carbon atom in the height direction by STM, the atom moved several tens of Å on the order of seconds [15]. A study of atomic force microscopy (AFM) observations found that one carbon atom continues to oscillate about 1 Å on the order of nanoseconds [16]. The TEM diffraction pattern revealed that the lattice vibration increases with increasing temperature [17].

Using ultrafast electron crystallography (UEC), two types of dynamic responses on the order of picosecond were elucidated [18].

Two kinds of methods using aberration-corrected electron microscopy have been reported for the 3D imaging of ripples in free-standing monolayer graphene. One kind includes scanning atomic electron tomography [19] and the measurement of the apparent shrinkage of the interstitial distance due to the slope on an atomic-resolution image of TEM/STEM [10,20]. The other kind uses the fact that the phase contrast of aberration-corrected TEM changes sensitively with respect to height or defocus [21,22]. In two reports, height was calculated from the intensity of one carbon atom and a monolayer graphene was 3D reconstructed with an accuracy within 1 Å [23,24]. However, the method can be applied only to an image acquired very close to the exact focus where the intensity is sensitive linearly to height differences; it becomes difficult to measure a ripple if the specimen fluctuates or tilts significantly.

In this paper, we propose a new method of measuring the quasi-static 3D structure of a pristine monolayer graphene. This method makes use of the height sensitivity of the phase contrast of the six-membered ring in an aberration-corrected TEM image. The atomic arrangement can be accurately reconstructed over a wide range of height changes without being significantly affected by specimen tilt. We have also devised a method of quantitatively analyzing the quasi-static 3D structure of graphene. This method revealed that a ripple can be represented as a superposition of sinusoidal waves, with their wave vectors coinciding approximately with the specific direction of the six-membered ring.

Materials and methods

Library of simulated images of six-membered rings

Using a flat monolayer graphene model, we constructed a library of 201 simulated images with defocus varying from -100 Å to +100 Å in 1 Å steps. The library was acquired using the multislice method (software: MacTempasX from HULINKS), which is an established wavefield calculation method for electron microscopy. The procedure is described as follows. First, the size of the supercell was set so that the size of one pixel coincided with the TEM image in the experiment. In the center of the supercell, a flat monolayer graphene with a nearest-neighbor atomic distance of 1.421 Å was placed with the rotation in the x-y plane aligned with the TEM image. In the simulation, the same acceleration voltage and aberration (spherical aberration, two-fold astigmatism, three-fold astigmatism, axial coma aberration) as in the observation conditions of the experiment were introduced, and the defocus was changed in steps of 1 Å. After Fourier inverse filtering with the first-order spots of 2.13 Å, each image for the library was made by cutting out a 3.22×3.22 Å^2 square containing the intensity around the six-membered ring. The fine structure, more so than the first-order spots, was hardly discernible in the experimental TEM image due to noise. Therefore, the experimental TEM images were filtered with the first-order spots to remove noise. Noise-free simulation images in the library were also filtered to intentionally cut higher-order structural information so as to meet each other's conditions.

Identification of the x-y-z coordinates of the six-membered ring

The x-y-z coordinates of the six-membered ring were identified by the following pattern-matching procedure. First, using a 2D TEM image, the coordinates were moved pixel by pixel, and 3.22×3.22 Å^2 images were cut out. Correlation values were calculated for all the cut-out TEM images and all the libraries of simulated images, and the maximum correlation value of each TEM image and its height z were obtained by selecting the corresponding simulated image with the highest correlation value. The zero-mean normalized cross-correlation (ZNCC) shown in the following equation was used as the function for obtaining the correlation value.

$$R_{f,g} = \frac{\sum_{x,y}\left(\left(f(\mathrm{x},\mathrm{y}) - \bar{f}\right)(g(\mathrm{x},\mathrm{y}) - \bar{g})\right)}{\sqrt{\sum_{\mathrm{x},\mathrm{y}}\left(f(\mathrm{x},\mathrm{y}) - \bar{f}\right)^2}\sqrt{\sum_{\mathrm{x},\mathrm{y}}(g(\mathrm{x},\mathrm{y}) - \bar{g})^2}}$$

Where $f(\mathrm{x},\mathrm{y})$ and $\bar{f}$ are the experimental intensity at (x,y) and the experimental average intensity, respectively. $g(\mathrm{x},\mathrm{y})$ and $\bar{g}$ correspond to the simulations.

A six-membered ring was placed at the coordinates where the correlation value is the local maximum. The height z of the arranged six-membered ring was determined at the same time. From the above, the x-y coordinates and height z of the six-membered ring were obtained in all the regions of the TEM image.

Preparation of free-standing graphene

We made free-standing graphene using a chemical vapor deposition (CVD) device and a recipe that we independently developed [25]. The detailed steps are described as follows. First, Cu foil (purity 99.8%) cut into a 1.5×1.5 cm^2 square was placed on a quartz plate and inserted into a quartz tube in the CVD device to grow graphene. The Cu foil had been immersed in acetic acid overnight to remove the natural oxide layer. The inside of the quartz tube was set to 60 kPa and 300° C, and Ar was introduced at 50 sccm for 15 minutes. The temperature inside the tube was then raised to 1000° C, and graphene was grown for 60 min in a 97.5 sccm Ar, 2 sccm H_2, 0.5 sccm CH_4 mixed gas flow. The copper was then rapidly cooled while the CH_4 flowed. Next, the graphene grown on the copper foil was floated on a mixed solution of sulfuric acid: hydrogen peroxide solution (3:1) in about 2 seconds, and only the backside Cu surface was etched. To dissolve the copper foil, it was floated on an ammonium persulfate aqueous solution for 4 hours. Finally, that solution was replaced with pure water, and the graphene was scooped up directly with a carbon-supported Cu TEM grid to prevent sample contamination. The TEM grid had been subjected to hydrophilization treatment for easy transfer.

TEM observation

The aberration-corrected TEM was a TITAN Cubed G2 60-300 manufactured by FEI. The accelerating voltage of the electron beam was set to 80 kV so that the graphene would not be damaged by knock-on [26]. First, the aberrations of the electron lens were corrected with amorphous carbon on the TEM grid. Based on the diffractogram tableau, spherical aberration was corrected to 0.0048 mm, and two-fold astigmatism, three-fold astigmatism, and axial coma aberration were also corrected to (Angle [°], Magnitude [Å]) = (-115.0, 40), (-100.0, 200), and (141.2, 72), respectively.

Through-focus TEM images were acquired as follows. The monolayer region in the specimen was searched using the electron diffraction pattern [3], and the exact focus was estimated by moving the defocus to where the contrast was smallest. Starting at the defocus, which was moved several tens of Å from the estimated exact focus to the underfocus (decreasing the excitation of the objective lens), a through-focus TEM image was acquired by moving the defocus to the overfocus side in steps of 5.26 Å (the error is ±0.1 Å), which is the device's minimum step size. The electron beam exposure time for acquiring a TEM image was set to 1 second, and the next TEM image was acquired after 4 seconds by moving the defocus. This procedure makes it possible to obtain through-focus TEM images including an exact focus.

In the experiment, it was carefully confirmed that aberrations were stable. The aberration coefficients were measured twice: before and after acquisition of the through-focus images. The dose of each TEM image was $1\sim2\times10^4\ e^{-1}/\text{Å}^2$.

Atomic force microscopy (AFM) observation

The topography of the free-standing graphene was observed by the cyclic contact mode of AFM (SPA-400, Hitachi High-Technologies Corporation) equipped with a closed-loop system. We used a silicon cantilever with a spring constant of 26 N/m (catalog value provided by the manufacturer). The Q value was controlled so that the excitation voltage was 0.3 V and the vibration amplitude was 1.0 V. AFM and TEM observations were made in almost, but not exactly, the same location.

Results and discussion

Proposed method and verification by numerical simulation

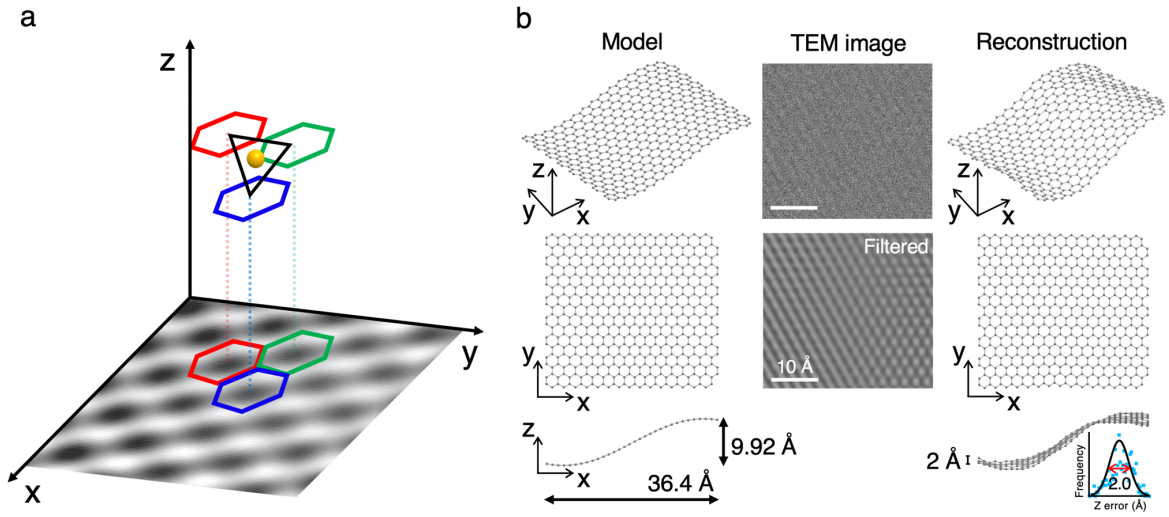

Figure 1. Proposed method and verification by numerical simulation.

a. Schematic of the proposed method for extracting the 3D positions of carbon atoms from a 2D TEM image. In the x-y plane, a 2D TEM image of a monolayer graphene and three adjacent six-membered rings (red, blue, green) extracted by pattern matching are shown. The height information for each six-membered ring is indicated by red, blue, and green dotted lines. The center of gravity of the triangle (black triangle) formed by connecting the centers of these three six-membered rings is the 3D position of the carbon atom (yellow sphere).

b. Verification of the proposed method by numerical simulation. On the left is a 3D atomic arrangement model of monolayer graphene with deformation in the z direction. The top, middle, and bottom are respectively drawn as an x-y-z 3D diagram, an x-y 2D projection diagram, and an x-z 2D projection diagram. For ease of viewing, each atom is connected by a line. The deformation was a sinusoidal wave ($z = \sin(2\pi x/60)$) with an amplitude of 5 Å and a wavelength of 60 Å. The

projected region in the x-y plane was 36.4×36.4 Å^2. The distance between the nearest-neighbor carbon atoms was set to 1.421 Å. The TEM image in the center is the simulated result (software: MacTempasX, HULINKS) considering the experimental conditions of aberration-corrected TEM. Above is an image in which noise has been introduced with a dose amount of 10^4 e^- / Å^2 after multislice calculation. Below is an image that has been filtered to remove noise from the image above. The filtered image was reconstructed three-dimensionally. On the right is the reconstructed result of the 3D carbon atomic arrangement obtained by the proposed method. At the bottom right, the height difference between each atom and the original model (that is, the z error) is shown as a histogram (blue dot), and the approximate curve of the Gaussian function (black solid line) is drawn.

We describe the proposed method of identifying the 3D arrangement of carbon atoms by using a 2D TEM image of a free-standing monolayer graphene. The method is divided into two processes. The first is to identify the 3D coordinates of each six-membered ring by pattern matching with the simulated image. The second is to arrange the carbon atoms in 3D.

Fig. 1a outlines the method. A 2D TEM image is shown in the x-y plane. As an example, three adjacent six-membered rings identified by pattern matching are also shown in red, blue, and green. The heights of these rings are indicated by dotted lines in the respective colors. One atom (yellow sphere) is arranged at the center of gravity of a triangle (black triangle) formed by connecting the centers of the three six-membered rings. This method of arranging carbon atoms was used by Y. Maehara et al. in 2D [27], and we applied it to 3D. This allows the 3D position (x,y,z) of one atom to be determined. By repeating the same operation for all three adjacent six-membered rings, the 3D positions of the carbon atoms can be reconstructed from the TEM image of the monolayer graphene obtained in the experiment.

Fig. 1b shows an example of the verification of the proposed method's effectiveness by using numerical simulation. The model on the left is a 3D atomic arrangement model of monolayer graphene with deformation in the z direction. Based on a report [3] that a ripple of the monolayer graphene is likely to be a wave, part of a sinusoidal wave with an amplitude of 5 Å and a period of 60 Å was used as an atomic model. The TEM image in the center is a simulated 2D TEM image using the experimental conditions of TEM observation at a dose of $1 \times 10^4\ e^{-1}/\text{Å}^2$ [28]. The noise was reduced from this image by Fourier inverse filtering with the first-order spots of 2.13 Å using a filter size of 3×3. The contrast differs between the left and right sides of the image. There are also subtle differences in contrast between adjacent six-membered rings. This indicates that the phase contrast of the TEM image reflects the height of each six-membered ring. The reconstruction

on the right shows the result of the 3D atomic arrangement obtained by the proposed method as explained in Fig. 1a. Comparison with the original model on the left shows almost no difference in the x-y projections but a slight difference in the x-y-z 3D image and in the x-z 2D projection. On the bottom right, the height error from the model for each atom is shown as a frequency distribution graph (histogram, blue dot), and the approximate curve (black solid line) of the Gaussian function is drawn. The height error can be approximated by a Gaussian function with a standard deviation of ±1.0 Å. Since the error in the x-y plane was less than 1 pixel (= 0.15 Å), the height error in the z direction was the dominant error in the reconstruction process. 3D structures such as inclined six-membered rings have not been considered. We used the 2D flat monolayer graphene model described in Materials and methods. This is valid from the results of the sine wave simulation shown in Fig. 1b. In this example, the maximum tilt angle is 16 degrees in the central region, but the height error is not the largest in this region. The error is due to noise.

TEM observation and image processing.

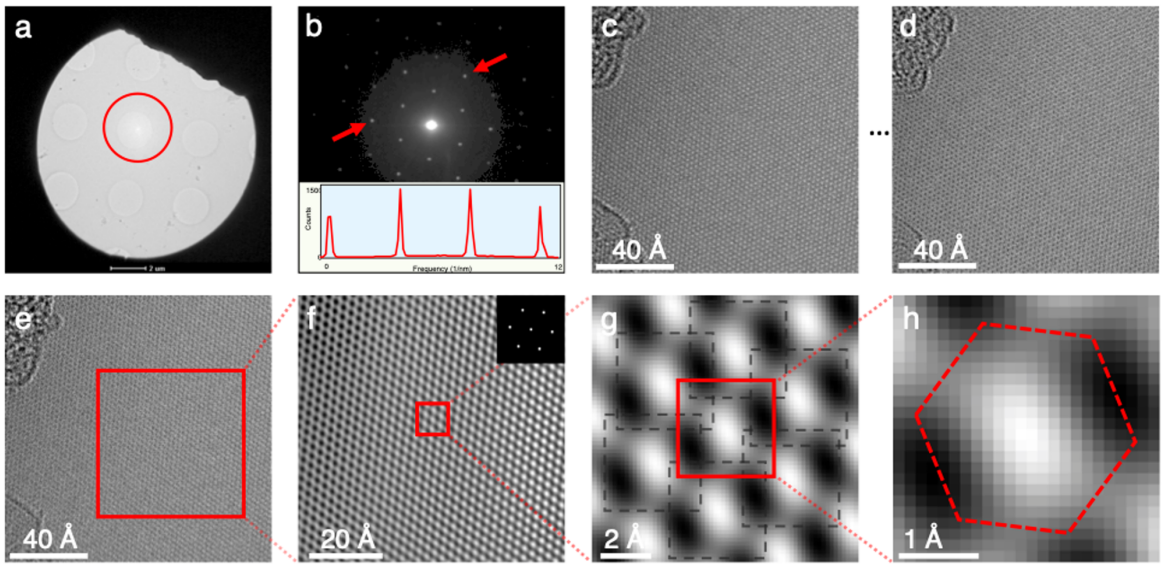

Figure 2. TEM observation and image processing.

a. Observed hole (red circle) in TEM grid.

b. Electron diffraction pattern at the hole in the red circle. Inset shows the intensity profile along the red arrows.

c, d. Through-focus TEM images (raw data) (c. TEM image 1, d. TEM image 15).

e. TEM image 6. Red square shows the region used for reconstruction.

f. TEM image after inverse Fourier transform using the filter in the inset.

g. Examples of identified six-membered rings. Red and black squares represent six-membered rings identified by pattern matching.

h. The red dotted line represents a six-membered ring with the nearest-neighbor atomic distance of 1.42 Å. There is a carbon atom at the intersection of each side.

An experiment using an aberration-corrected TEM was performed to obtain the 3D reconstruction of monolayer graphene by the proposed method. To compare the experimental and simulated images over a wide defocus range, a series of through-focus TEM images were acquired. Specimen preparation and TEM observation are described in the Materials and methods section.

Fig. 2a shows an observed hole (red circle) in the TEM grid. Fig. 2b shows the selected-area electron diffraction pattern with a diameter of about 126 nm and its intensity profile. The two inner (first-order) diffraction spots are larger than the outer (second-order) spots. In the case of monolayer graphene, the first-order diffraction spot of the electron diffraction pattern is larger than the second-order spot [29]. Fig. 2c and 2d are examples of the acquired through-focus 15 TEM images. Next, drift correction was performed on each acquired through-focus image, and a pristine region in Fig. 2e was cut into an area of 72.76×72.76 Å^2. Fig. 2f shows the TEM image after inverse Fourier transform using the filter in the inset. The S/N ratio was improved by extracting only the first-order spots by filtering. Fig. 2g shows examples of an identified six-membered ring by pattern matching as presented in the Materials and methods section. Fig. 2h represents a six-membered ring. There is a carbon atom at the intersection of each side.

Subsequently, 3D reconstruction of the atomic arrangement was performed on the 15 TEM images. Hereinafter, they are referred to as TEM image 1, TEM image 2,... TEM image 15 in the order of acquisition.

Comparison of experiment and simulation for a six-membered ring

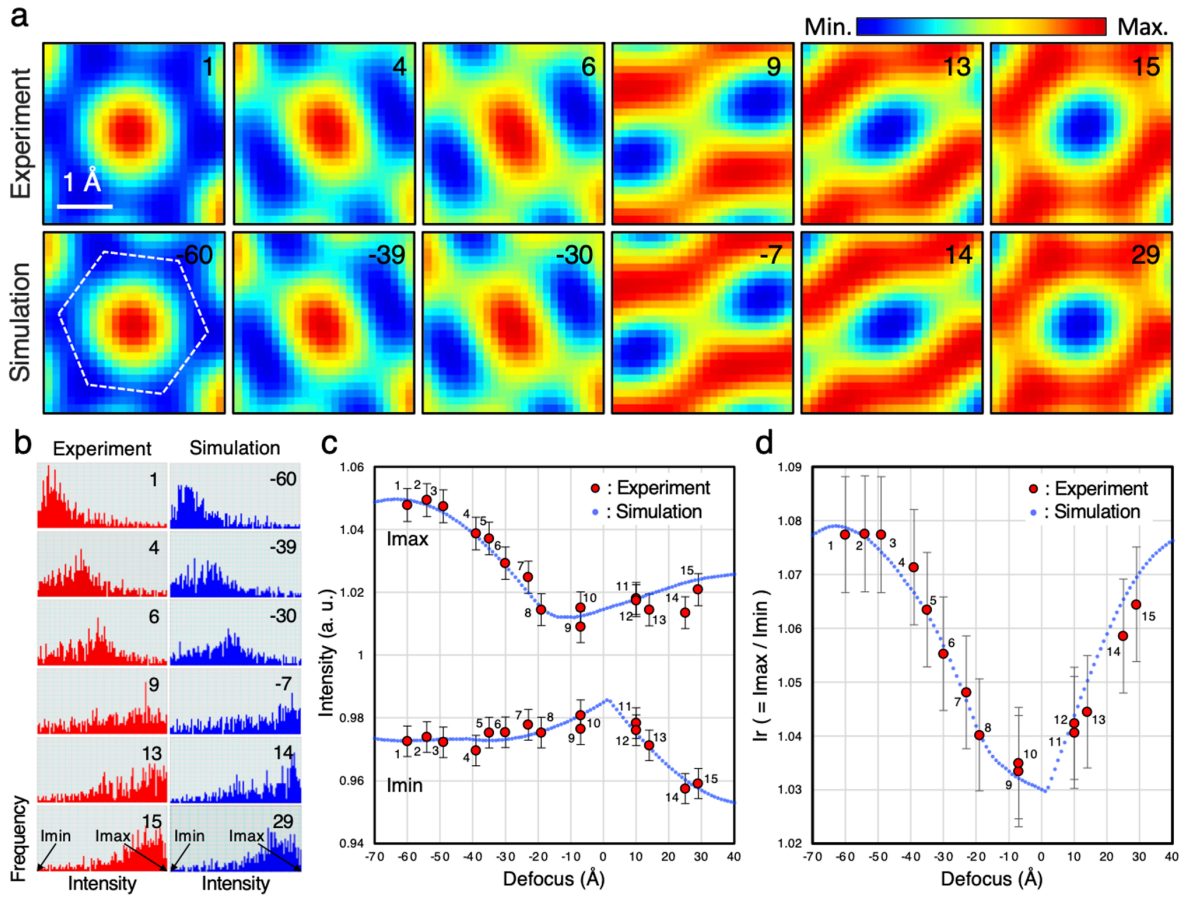

Figure 3. Comparison of experiment and simulation for a six-membered ring.

a. The upper images show experimental through-focus TEM images cut out with the six-membered ring (size of 3.22 × 3.22 Å^2, 24 × 24 pixels, 6 of 15 images, pseudo-color display). The number in the upper right of each TEM image indicates the order in which the image was acquired. For example, the image of the number 6 corresponds to the TEM image 6. Each image shows the center of the whole TEM image from which it was derived at the position indicated by the red square in Fig. 2g. Lower images are simulated images that show the highest correlations with the upper images. The number in the upper right is the defocus value (Å). As a guide, a six-membered ring

with a nearest-neighbor atomic distance of 1.42 Å is drawn in the simulated image at the left end with a dotted white line. There is a carbon atom at the intersection of each side.

b. Intensity distribution of the images in Fig. 3a. The results of the experiment (red) and simulation (blue) are drawn. The horizontal and vertical axes represent the pixel intensity and frequency, respectively. The both sides of the horizontal axes are the maximum intensity (Imax) and the minimum intensity (Imin), respectively.

c. Defocus dependence of Imax and Imin. These intensities are the minimum and maximum intensities of each six-membered ring. The blue circles in 1 Å steps represent the simulated result and the other 15 red circles represent the experimental result. Error bars were estimated from statistical error at a dose of $1.0 \times 10^4\ e^{-1}/\text{Å}^2$.

d. Defocus dependence of the intensity ratio (Ir) defined as Ir = Imax/ Imin. The Ir was calculated using Fig. 3c. The blue and red circles are drawn in the same way as in Fig. 3c.

Fig. 3a shows examples of through-focus TEM images of the six-membered ring (upper images) and the corresponding simulated images (lower images). It can be seen that the 2D contrast patterns of TEM images were in good agreement with the simulated images. Details on how to determine the defocus value of the six-membered ring are shown in Fig. S1. The results of all 15 TEM images of the six-membered ring are shown in Fig. S2. The correlation values defined in the Materials and methods section were above 0.95 over a wide defocus range of 89 Å. In Fig. 3a, from left to right, as the focus shifted to overfocus, the intensity of the carbon atoms increased and the intensity of the center of the six-membered ring decreased. It should be noted here that the six-fold symmetry was broken for any defocused TEM image of the six-membered ring. This is due to the residual aberrations of two-fold and three-fold astigmatisms. Through-focus TEM images were acquired with each defocus in steps of 5.26 Å, but the step size of the highly correlated simulated images does not match 5.26 Å. This is because the specimen was moving. We describe this in detail in Fig. 4.

Fig. 3b shows the intensity distribution of the images in Fig. 3a. The results of all 15 intensity distributions of the TEM images are shown in Fig. S3. Fig. 3c shows the defocus dependence of the maximum intensity (Imax) and the minimum intensity (Imin). The experiment and simulation were confirmed to be in good agreement within the error. Fig. 3d shows the defocus dependence of the intensity ratio (Ir). In the simulation (blue dots), it can be seen that Ir is the minimum at defocus = 1 Å. In the ideal case where the aberration is zero, the minimum Ir is at the exact focus, i.e. defocus = 0 Å, but in this experiment, the minimum Ir deviates from zero defocus due to the slight residual aberration. The Ir of the experimental TEM images 1 ~ 10 were plotted on the underfocus side, and those of the TEM images 11 ~ 15 were plotted on the overfocus side with the exact focus in between.

3D Reconstruction of atomic arrangement and AFM measurement

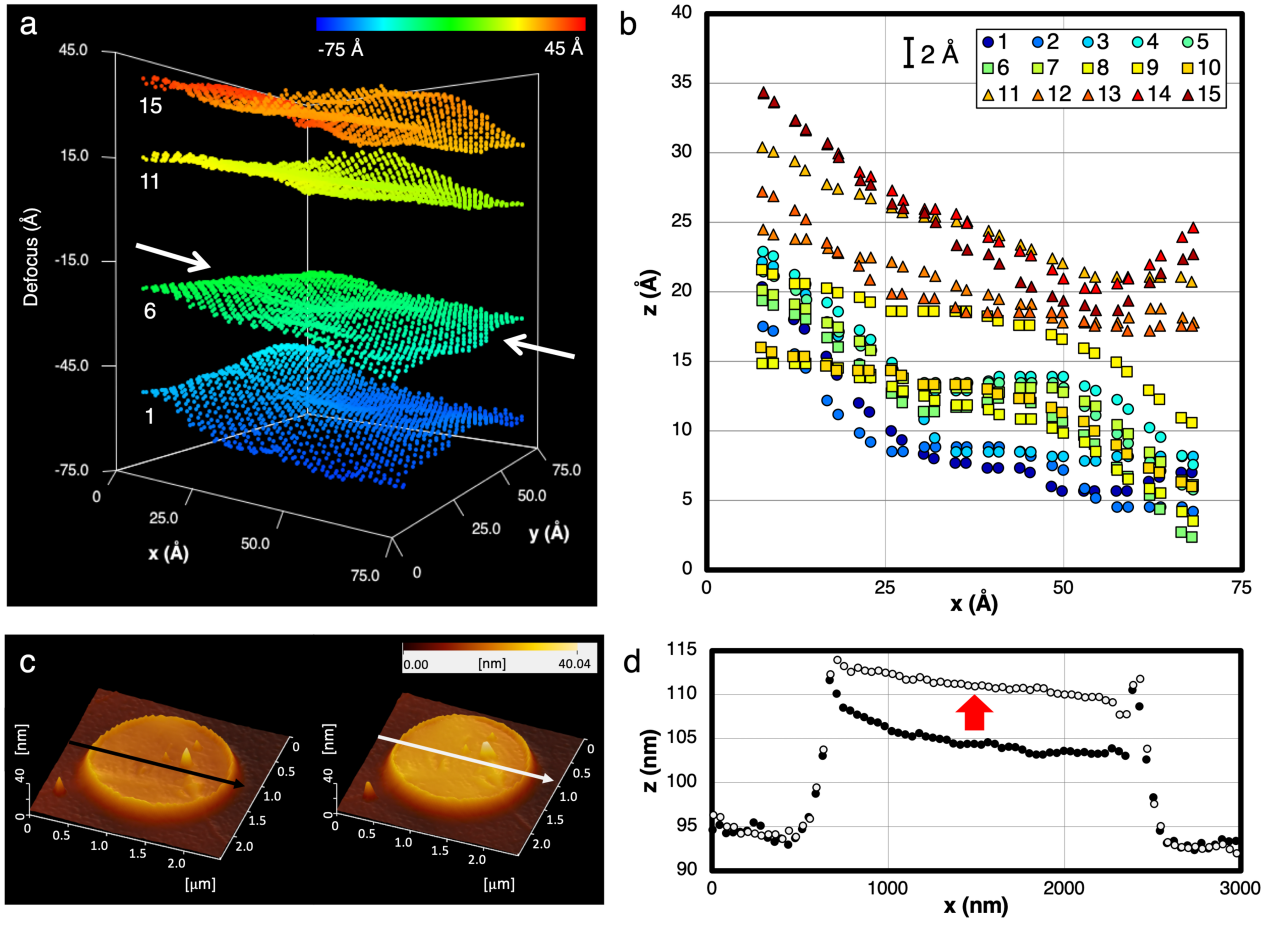

Figure 4. 3D Reconstruction of atomic arrangement and AFM measurement.

a. From the bottom, the 3D reconstruction results of TEM images 1, 6, 11, and 15 are drawn. The plot represents carbon atoms. The vertical axis is the defocus (Å), and the carbon atom is colored by the color bar in the upper right according to the defocus.

b. For all 15 TEM images, the x-z positions of carbon atoms are plotted in the cross section indicated by the white arrows in Fig. 4a. In the figure, the defocus when the through-focus image

was acquired is subtracted, so that the vertical axis shows height z itself. The lowest carbon atom of TEM image 1 was set to 0. The colors of plots in the figure indicate acquisition times. The error bar was 2 Å from the result shown in Fig. 1b.

c. AFM images of holes with graphene transferred (left and right: before and after TEM observation, respectively).

d. Cross-sectional profile along the straight line indicated by the black and white arrows in the AFM image of Fig. 4c (black and white plots: before and after TEM observation, respectively). The horizontal axis is x and the vertical axis is z. As shown by the red arrow, the entire cross section rose by about 6 nm.

The 15 through-focus TEM images were reconstructed in 3D. Fig. 4a shows the 3D reconstruction results obtained from TEM images 1, 6, 11, and 15. The vertical axis is the defocus. Atoms are arranged smoothly in each image. Although they are from the same specimen, they have different 3D structures. All 3D reconstruction images are listed in Fig. S4. It is possible for the structure to change even during the acquisition of a single image, but an average structure or a structure with a long stay time for 1 s appears as the reconstruction image. This indicates that the graphene obtained in this experiment has a quasi-static 3D structure.

Fig. 4b shows cross sections of the 15 3D structures, in which are plotted the carbon atoms in the cross section indicated by the white arrows in Fig. 4a. The same carbon atoms are drawn in all the cross sections of all 15 through-focus TEM images. The vertical axis of each cross section was converted to height z by removing 5.26 Å, which was moved step by step during the acquisition of the through-focus TEM images, from the defocus value of each carbon atom. Cross section 1 was located at z = 5 ~ 20 Å, while cross section 15 was located at z = 20 ~ 35 Å. This indicates that the specimen rose 15 ~ 20 Å during TEM observation (about 70 seconds). This is why the step width of defocus in Fig. 3a is not equal to 5.26 Å. In addition, all cross sections had a negative slope with respect to the x-axis. For example, in TEM image 6, the tilt angle is about 16 degrees.

Figs. 4a and 4b revealed not only that the 3D structure varied but also that the specimen moved in one direction. The latter was observed by AFM before and after the TEM observation. Fig. 4c shows an example of AFM measurements, and Fig. 4d is a cross-sectional view. The AFM experimental method is described in the Materials and methods section, and Fig. S5 shows additional measurements to confirm that the AFM itself is not causing morphological changes in the graphene. As shown by the red arrow in Fig. 4d, the entire graphene rose by about 6 nm (from

1 the black plot to the white plot). The results obtained from AFM are consistent with those in Fig.
2 4b obtained by TEM and strongly support that the whole graphene rose during TEM observation.
3 However, note that under the measurement conditions this time, the resolution in the x-y plane of
4 AFM was ±10 nm, which is significantly different from that of TEM. It is considered that the
5 specimen drift in the z direction is attributable to factors in the environment inside the TEM facility,
6 such as the influence of electron beam irradiation and the direction of vacuuming. However, much
7 more careful examination is needed to arrive at a physical explanation of the specimen drift in the
8 z direction.
9

Approximation of 3D atomic arrangement

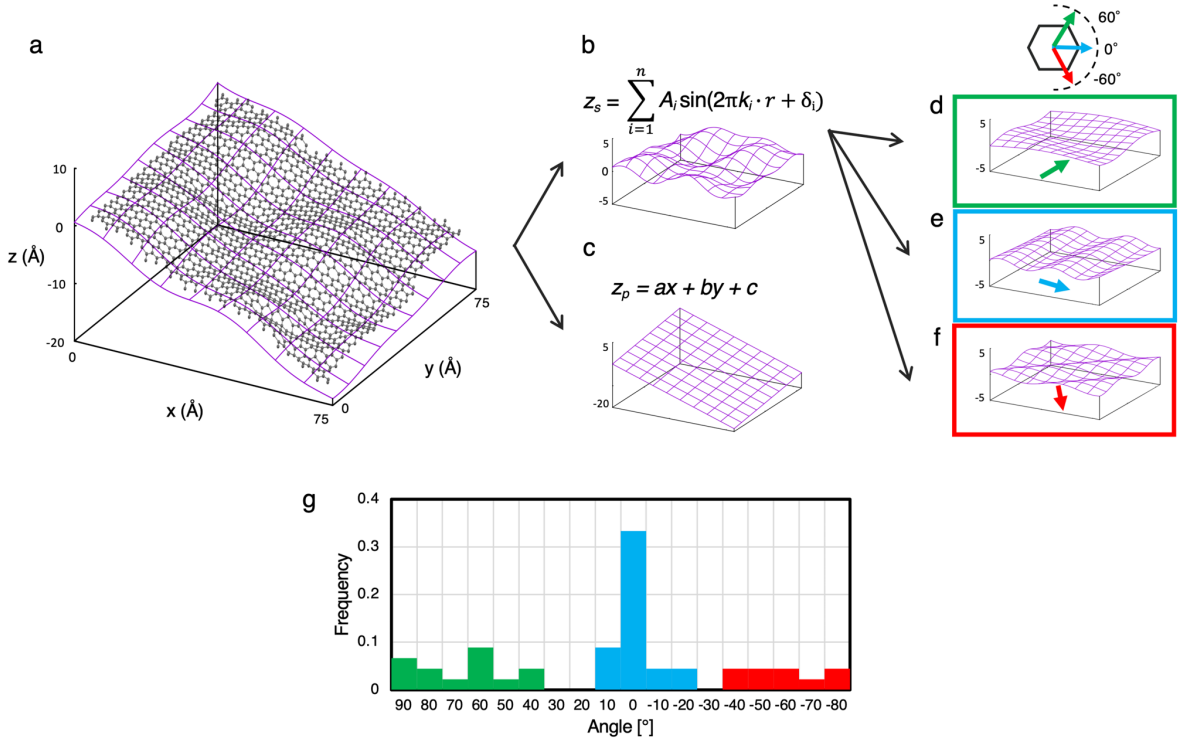

Figure 5. Approximation of 3D atomic arrangement (TEM image 6 as an example) and directions of the sinusoidal waves.

a. The reconstructed atomic arrangement (black) and the approximated curved surface (purple).

b, c. Sinusoidal and plane components.

d, e, f. Three constituent sinusoidal waves of the sinusoidal component. The green, blue, and red arrows indicate the directions of the respective sinusoidal waves.

g. A histogram of all directions of the 45 (3×15) sinusoidal waves. The horizontal axis of the graph shows the angle (°), and the vertical axis shows the frequency.

We considered approximating the reconstructed atomic arrangement in Fig. 4a as a composite of two functions with multiple sinusoids (z_s) and one plane (z_p) as follows.

$$z = z_s + z_p$$
$$= \sum_{i=1}^{n} \{A_i sin(2\pi k_i \cdot r + \delta_i)\} + ax + by + c$$
$$k_i = (k_{xi}, k_{yi}, k_{zi}), r = (x, y, z).$$

Where A_i, k_i, r, and δ_i are the amplitude, wave vector, position vector, and phase, respectively; a, b, c are the linear coefficients of z_p. The function had parameters $(A_i, k_i, \delta_i, a, b, c)$ that minimize the squared error per atom.

Fig. 5 shows an example of the approximation. Fig. 5a shows the approximated curved surface and the reconstruction of TEM image 6 in Fig. 4a. It can be seen that they agree very well. The average height error per carbon atom of the approximation was ±0.62 Å. Figs. 5b and 5c show structures of the sinusoidal term z_s and of the plane term z_p. In this paper, the structure of the sinusoidal term z_s is defined as a ripple. From Fig. 5b, a min-max height difference of 3.6 Å was found in the 72.76×72.76 Å^2 region, and from Fig. 5c we see that it was tilted by 14.0° in the x direction and 4.4° in the y direction. The results in Fig. 5c are in quantitative agreement with the tilt angles in Fig. 4b. This shows that the approximation can clearly divide a structure with a ripple and a slope. Figs. 5d ~ 5f show the three sinusoidal waves that compose the ripple shown in Fig. 5b. These waves correspond to the directions of the green, blue, and red arrows, and their amplitudes and wavelengths were (0.68 Å, 65.8 Å), (0.68 Å, 35.7 Å), and (0.54 Å, 32.5 Å), respectively. It was found that the three directions corresponded to those of the six-membered ring (upper diagram in Fig. 5d).

For the approximation of 15 reconstructions, Fig. S6 shows how the average error per atom decreased as the number of sinusoidal waves used for interpolation increased. The results,

combined with the finding that the standard deviation of the height error was 1 Å in the numerical simulation shown in Fig. 1b, allowed us to estimated that the approximation with three or four sinusoidal waves is appropriate. Fig. S7 shows the ripples, i.e., the structures of the sinusoidal term z_s, of all 15 reconstructed structures with three sinusoidal waves. Some of the 15 ripples show similar 3D structures in two adjacent ones (1 and 2, 4 and 5, 8-10, etc., with peaks and valleys in the close positions). In addition, Fig. 5g shows a histogram of all directions of the 45 ($=3 \times 15$) sinusoidal waves. It was revealed that three directions were dominant in all 15 approximations and that each ripple was composed of waves in two or three specific directions of the six-membered ring. Because there are areas where no color exists between colors, it turns out that there is a clear boundary. The preference for the zero angle direction may be attributable to contamination, distortion outside the reconstructed field of view, or the tension from boundaries that support graphene. However, further experiments are needed to clarify these reasons.

Height and lateral size of the ripple structure

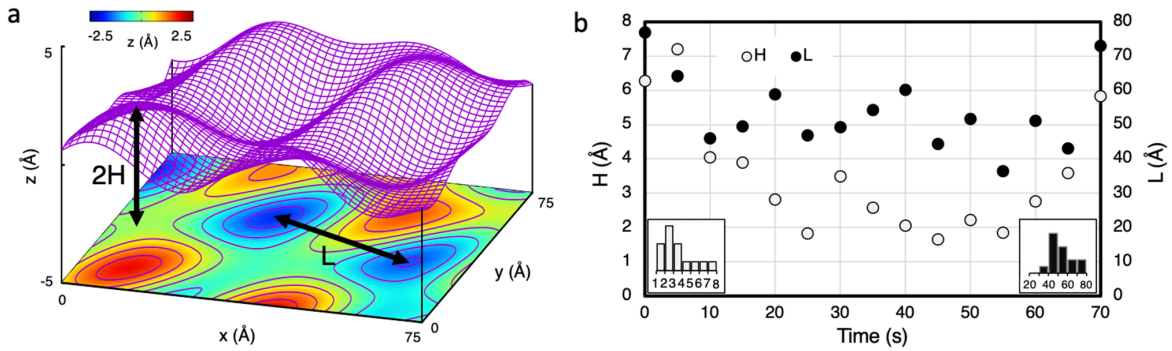

Figure 6. Height and lateral size of the ripple structure.

a. Definitions of height (H) and lateral size (L). With the same curved surface as shown in Fig. 4b, contour lines are drawn in the x-y plane. The definitions of 2H and L are shown by black arrows.

b. Time dependence of H and L. H and L were obtained from all 15 approximation results and plotted on a graph whose horizontal axis represented time. The white plot is H and the black plot is L. The insets in the lower left and lower right show the frequency distributions of H and L, respectively (the unit of the horizontal axis is Å).

Finally, we investigated the time variations of height (H) and lateral size (L) for the ripple structure. Fig. 6a shows the definitions of H and L of the ripple. 2H is the difference between the maximum and minimum values of z, and height H is defined as half of that. In the case of the ripple structure in Fig. 6a, the maximum value was z = 1.84 Å and the minimum value was z = -1.80 Å, so that H was (1.84 - (-1.80))/2 = 1.82 Å. L is defined as the average for all combinations of the distances between the maximum points (peaks) or the minimum points (valleys) in the whole region. The ripple in Fig. 6a shows three local maxima indicated by red peaks and three local minima indicated by blue peaks of the contour line. Therefore, calculation of the average for 6 (3 combinations to select 2 from 3 convex, 3 combinations to select 2 from 3 concave, total 6 average) different distances revealed that L of the ripple structure was 46.9 Å.

From theses above definitions, H and L were calculated for all 15 reconstruction results. Fig. 6b shows the time dependence of H and L. H and L changed randomly at 5-second intervals. Furthermore, the frequency distributions of H and L are shown in Fig. 6b. H had a distribution in the range of 1.7 to 7.2 Å. L had a distribution in the range of 36 to 77 Å. The ratio H/L varied by 0.03 ~ 0.11. The ratio was quantitatively consistent with those in some reports but not with those in others [3,4,23,24,30]. This may be due to differences in conditions, such as sample size, from study to study [3].

Conclusion and discussion

We presented a new method for the 3D reconstruction of a ripple from a single 2D TEM image. First, numerical simulation verified that the method is capable of 3D reconstruction with a z error within ±1 Å per carbon atom. Next, using an aberration-corrected TEM, 15 through-focus images were acquired during 70 seconds for a wide defocus range of about 100 Å. There are two reasons to use through-focus images. One is that it is necessary to clearly show that the contrast matches between the experimental and simulated six-membered rings. The other reason is to experimentally show the range of defocus to which this method can be applied. The 2D contrast of the TEM images of the six-membered ring was in good agreement with that of the simulated images. The 3D atomic arrangements of consecutively acquired TEM images were reconstructed. Furthermore, by approximating the obtained 3D reconstructed graphene with multiple sinusoidal waves and a plane function, we were able to cleanly separate the slope component and the ripple component. A true ripple structure was obtained by removing tilt and drift in the z direction, which were problems in high-resolution imaging using aberration-corrected electron microscopy. Moreover, the ripple in graphene was found to consist of the superposition of three or four sinusoidal waves approximately coinciding with the specific direction of the six-membered ring.

Since this method uses the six-membered ring as the basic unit, local defects such as dislocations and voids make it difficult to calculate the height without modeling defects where the six-membered ring is broken. In that case, it would be effective to complementarily use the method of locally calculating the height accurately from the TEM intensity of a single atom [23,24]. An experimentally important parameter that limits accuracy is the signal-to-noise ratio (S/N). The electron dose in the experiment was $1\sim2\times10^4\ e^{-1}/\text{Å}^2$ during an exposure time of 1 second. S/N can be improved by using multiple six-membered rings for pattern matching. This reduces the

resolution in the x-y plane but improves height accuracy. In fact, it has been reported that the large size accurately determines the ripple of few-layer graphene [31], although not that of monolayer graphene.

The 3D reconstruction method proposed in this paper can be applied to other 2D materials. In addition, we expect it to be used widely to elucidate the basic properties of 2D materials and to control those materials.

Associated content

Supporting Information. Detail of TEM image acquisition, all data on through-focus TEM images and simulated images, all data on 3D reconstructions and approximations by sinusoidal waves, detailed results of the analysis (PDF).

Conflict of Interest: The authors declare no competing financial interest.

Acknowledgment. This work was partly supported by a JSPS Grants-in-Aid for Scientific Research (grant numbers 26105009, 19K1543909, 16K13688). Part of this work was conducted at Hokkaido University and was supported by the Nanotechnology Platform Program of the Ministry of Education, Culture, Sports, Science, and Technology (MEXT), Japan. J.Y. thanks Prof. K. Saitoh and Dr. C. Cassidy for their discussions.

Author Contributions

Y.S. and K.G. conceived the idea and designed the study. Y.S. and K.Y. prepared the samples for the experiments and performed the TEM and AFM observations. Y.S. performed the numerical simulations. Y.S. and K.G. analyzed the data. Y.S. and K.G. wrote the manuscript, and all authors commented on it.

References

1 K. S. Novoselov, A. K. Geim, S. V. Morozov, D. Jiang, Y. Zhang, S. V. Dubonos, I. V. Grigorieva and A. A. Firsov, *Science*, 2004, **306**, 666–669.

2 S. Deng and V. Berry, *Mater. Today*, 2016, **19**, 197–212.

3 J. C. Meyer, A. K. Geim, M. I. Katsnelson, K. S. Novoselov, T. J. Booth and S. Roth, *Nature*, 2007, **446**, 60–63.

4 A. Fasolino, J. H. Los and M. I. Katsnelson, *Nat. Mater.*, 2007, **6**, 858–861.

5 F. De Juan, A. Cortijo and M. A. H. Vozmediano, *Phys. Rev. B - Condens. Matter Mater. Phys.*, 2007, **76**, 165409.

6 R. J. T. Nicholl, H. J. Conley, N. V. Lavrik, I. Vlassiouk, Y. S. Puzyrev, V. P. Sreenivas, S. T. Pantelides and K. I. Bolotin, *Nat. Commun.*, 2015, **6**, 8789.

7 P. Z. Sun, Q. Yang, W. J. Kuang, Y. V. Stebunov, W. Q. Xiong, J. Yu, R. R. Nair, M. I. Katsnelson, S. J. Yuan, I. V. Grigorieva, M. Lozada-Hidalgo, F. C. Wang and A. K. Geim, *Nature*, 2020, **579**, 229–232.

8 Y. Liu and B. I. Yakobson, *Nano Lett.*, 2010, **10**, 2178–2183.

9 J. H. Warner, E. R. Margine, M. Mukai, A. W. Robertson, F. Giustino and A. I. Kirkland, *Science*, 2012, **337**, 209–212.

10 J. H. Warner, Y. Fan, A. W. Robertson, K. He, E. Yoon and G. Do Lee, *Nano Lett.*, 2013, **13**, 4937–4944.

11 E. Stolyarova, T. R. Kwang, S. Ryu, J. Maultzsch, P. Kim, L. E. Brus, T. F. Heinz, M. S. Hybertsen and G. W. Flynn, *Proc. Natl. Acad. Sci. U. S. A.*, 2007, **104**, 9209–9212.

12 M. Ishigami, J. H. Chen, W. G. Cullen, M. S. Fuhrer and E. D. Williams, *Nano Lett.*, 2007, **7**, 1643–1648.

13 U. Ludacka, M. R. A. Monazam, C. Rentenberger, M. Friedrich, U. Stefanelli, J. C. Meyer and J. Kotakoski, *npj 2D Mater. Appl.*, 2018, **2**, 25,

14 R. Zan, C. Muryn, U. Bangert, P. Mattocks, P. Wincott, D. Vaughan, X. Li, L. Colombo, R. S. Ruoff, B. Hamilton and K. S. Novoselov, *Nanoscale*, 2012, **4**, 3065–3068.

15 P. Xu, M. Neek-Amal, S. D. Barber, J. K. Schoelz, M. L. Ackerman, P. M. Thibado, A. Sadeghi and F. M. Peeters, *Nat. Commun.*, 2014, **5**, 1–7.

16 M. L. Ackerman, P. Kumar, M. Neek-Amal, P. M. Thibado, F. M. Peeters and S. Singh, *Phys. Rev. Lett.*, 2016, **117**, 1–5.

17 C. S. Allen, E. Liberti, J. S. Kim, Q. Xu, Y. Fan, K. He, A. W. Robertson, H. W. Zandbergen, J. H. Warner and A. I. Kirkland, *J. Appl. Phys.*, 2015, **118**, 74302.

18 J. Hu, G. M. Vanacore, A. Cepellotti, N. Marzari and A. H. Zewail, *Proc. Natl. Acad. Sci. U. S. A.*, 2016, **113**, E6555–E6561.

19 X. Tian, D. S. Kim, S. Yang, C. J. Ciccarino, Y. Gong, Y. Yang, Y. Yang, B. Duschatko, Y. Yuan, P. M. Ajayan, J. C. Idrobo, P. Narang and J. Miao, *Nat. Mater.*, 2020, **19**, 867–873.

20 U. Bangert, M. H. Gass, A. L. Bleloch, R. R. Nair and A. K. Geim, *Phys. Status Solidi Appl. Mater. Sci.*, 2009, **206**, 1117–1122.

21 K. Hirahara, K. Saitoh, J. Yamasaki and N. Tanaka, *Nano Lett.*, 2006, **6**, 1778–1783.

22 D. Van Dyck, J. R. Jinschek and F. R. Chen, *Nature*, 2012, **486**, 243–246.

23 L. G. Chen, J. Warner, A. I. Kirkland, F. R. Chen and D. Van Dyck, *Sci. Rep.*, 2017, **7**, 10839

24 S. Morishita, R. Senga, Y. C. Lin, R. Kato, H. Sawada and K. Suenaga, *Appl. Phys. Lett.*, 2018, **113**, 233101.

25 K. Yamazaki, Y. Maehara and K. Gohara, *J. Phys. Soc. Japan*, 2018, **87**, 1–6.

26 J. C. Meyer, C. Kisielowski, R. Erni, M. D. Rossell, M. F. Crommie and A. Zettl, *Nano Lett.*, 2008, **8**, 3582–3586.

27 Y. Maehara, K. Yamazaki and K. Gohara, *Carbon N. Y.*, 2019, **143**, 669–677.

28 J. C. Meyer, J. Kotakoski and C. Mangler, *Ultramicroscopy*, 2014, **145**, 13–21.

29 J. C. Meyer, A. K. Geim, M. I. Katsnelson, K. S. Novoselov, D. Obergfell, S. Roth, C. Girit and A. Zettl, *Solid State Commun.*, 2007, **143**, 101–109.

30 V. Geringer, M. Liebmann, T. Echtermeyer, S. Runte, M. Schmidt, R. Rückamp, M. C. Lemme and M. Morgenstern, *Phys. Rev. Lett.*, 2009, ***102***, 076102.

31 W. L. Wang, S. Bhandari, W. Yi, D. C. Bell, R. Westervelt and E. Kaxiras, *Nano Lett.*, 2012, **12**, 2278–2282.

1